Kink ordering and organized growth of Co clusters on a stepped Au(111) surface: A combined grazing-incidence x-ray scattering and STM study

Frédéric Leroy,[1,*] Gilles Renaud,[2] Antoine Létoublon,[3] Stanislas Rohart,[4,5] Yann Girard,[5] Vincent Repain,[5] Sylvie Rousset,[5] Alessandro Coati,[6] and Yves Garreau[5,6]

[1]*Centre de Recherche en Matière Condensée et NanoSciences, CNRS-UPR 7281, Campus de Luminy Case 913, 13288 Marseille, Cedex 09, France*

[2]*Commissariat à l'Energie Atomique, Département de Recherche Fondamentale sur la Matière Condensée, Service de Physique des Matériaux et Microstructures, Nanostructures et Rayonnement Synchrotron, 17, Avenue des Martyrs, F-38054 Grenoble, Cedex 9, France*

[3]*Laboratoire d'Etude des Nanostructures Semiconductrices, INSA-Rennes, 20, Avenue des buttes de Coesmes, CS 14315, 35043 Rennes Cedex, France*

[4]*Laboratoire de Physique des Solides: UMR 8502, Université Paris-Sud, Bâtiment 510, 91405 Orsay Cedex, France*

[5]*Matériaux et Phénomènes Quantiques: Universités Paris 7, CNRS UMR 7162, 2, Place Jussieu, 75251 Paris Cedex, France*

[6]*Synchrotron SOLEIL: L'Orme des Merisier, Saint-Aubin, BP 48, 91192 Gif-sur-Yvette, France*

(Received 30 July 2007; revised manuscript received 5 October 2007; published 29 January 2008)

The surface topography of a kinked vicinal surface of Au(111) is characterized by *in situ* grazing incidence small-angle x-ray scattering and scanning tunneling microscopy. The step edges exhibit a long range ordering of kinks which is attributed to the repulsive interaction between the kinks and the surface reconstruction. The kink size and ordering are revealed by three-dimensional measurements of the reciprocal space close to the origin and by a detailed analysis performed in the framework of the ideal paracrystal model. The growth of Co clusters on this surface gives rise to a long-range ordering induced by the surface reconstruction and revealed by the interferences between the x-ray waves scattered by the steps and/or kinks and by the Co clusters. These results are completed with *in situ* grazing incidence x-ray diffraction measurements, providing a crystallographic description of the Co clusters.

DOI: 10.1103/PhysRevB.77.045430 PACS number(s): 61.46.−w, 61.05.cf, 68.35.B−, 68.55.A−

I. INTRODUCTION

Growing identical nanostructures on a surface is of great interest both for applied and fundamental physics. In that view, the use of spontaneously prepatterned substrates at the nanometer scale is a promising way to induce the nucleation and growth of clusters on specific sites. This approach not only leads to a regular network of clusters, but also to a narrow size distribution and, thus, to well defined properties.[1–5] Many different attempts of organized growth on prepatterned surfaces have been performed using dislocations, facets, or surface reconstructions. Among them, the growth of Co clusters on the Au(111) reconstruction is one of the most famous example of ordered growth on metal surfaces.[6] The reconstruction of the Au(111) surface relieves the stress due to the low coordination of the top atomic layer and provides preferential nucleation and growth sites for Co. The main advantages of the Au(111) reconstruction over other prepatterned surfaces are its large unit cell ($\simeq 15 \times 7$ nm^2) and its robustness in temperature. However, the growth is well ordered only over areas of $\sim 100 \times 100$ nm^2. At larger scales, different variants of the so-called herringbone surface reconstruction coexist, thus limiting the long-range order. Moreover, defects, mainly steps, affect the coherence of the network. The use of vicinal surfaces of Au(111) allows us to overcome both drawbacks of the nominal surface. Breaking the symmetry, only one variant of the reconstruction is favored and steps are now ordered and participate in the patterning of the surface.[7] The terrace width can be tuned to adapt the patterning periodicity[8] provided that (i) the terraces are wide enough to develop the reconstruction[7] [e.g., Au(322), Au(755), and Au(233) are unreconstructed], (ii) the distance between steps is small enough to allow elastic interactions between steps to organize them in a regular staircase,[9] and (iii) the surface is stable against faceting.[7,10] For instance, vicinal surfaces misoriented toward $[2\bar{1}\bar{1}]$ ({100} step edges) undergo usually a faceting [e.g., Au(433), Au(11 9 9), and Au(12 11 11)], whereas for opposite azimuth angles ($[\bar{2}11]$, {111} step edges), surfaces are stable between 2.2° and 4° misorientation angle. Therefore, the vicinal surfaces must exhibit {111} step edges,[7,11] and the terrace width can be tuned from 3.4 nm (4°) for the Au(677) surface to 5.8 nm (2.2°) for the Au(11 12 12) surface.

In the present work, we have studied the kink ordering along the step edges of a vicinal surface of Au(111) close to a Au(677) surface, which, in addition, was slightly disoriented azimuthally. A strong interplay between the kinks and the surface reconstruction is put in evidence. This interaction gives rise to a well-ordered two-dimensional (2D) network of kinks. Then this substrate has been used as a template for the organized growth of Co clusters. The nucleation sites of the clusters are located close to the crossing between the step edges and the reconstruction, and show a long-range ordering. The surface topography of the bare substrate (kinks and steps), and then the position and the size of the Co clusters are highlighted by the complementary use of scanning tunneling microscopy (STM) and *in situ* grazing incidence small-angle x-ray scattering (GISAXS).[12] The former provides in real space details of the local surface topography, whereas the latter reveals in reciprocal space the main surface features. The main drawbacks of near field microscopy

are the lack of knowledge of the tip interaction with the surface and the convolution effect of the tip with the surface. On the contrary, x-ray scattering techniques are quantitative tools as the scattering process is well described through the Born approximation (or distorted wave Born approximation[13]), which results from the very weak scattering cross section of x-ray with matter. The use of real space imaging techniques is, however, the key point to build a realistic model of the surface and to guide the quantitative analysis of the x-ray scattering data.

In that view, the topography of the bare surface is first studied by scanning tunneling microscopy. Then a three-dimensional (3D) map of reciprocal space is measured by GISAXS, and the result is analyzed quantitatively from a detailed 3D model of the surface topography developed thanks to the microscopy images. This model is based on the paracrystal theory,[14] with an appropriate choice of the elementary unit. It is revealed that kinks are long-range ordered along the step edges and from step to step. From STM and GISAXS data, we show that this behavior is induced by a kink-reconstruction interaction. Concerning the ordered growth of Co clusters, the long-range ordering of kinks and steps provides a powerful tool to localize the Co clusters thanks to the interferences between the waves scattered by the surface topography (steps and kinks) and those scattered by the Co clusters. Finally, complementary *in situ* grazing incidence x-ray diffraction (GIXD) measurements have been performed on the same sample at different stages of the Co growth. The crystallographic structure and the relaxation of the lattice parameter of the Co clusters and film are characterized as a function of deposit.

II. EXPERIMENTAL METHODS

The vicinal surface of Au(111) was prepared in ultrahigh vacuum (UHV) by cycles of ion bombardment and annealing. Ion bombardment was performed with Ar^+ (1 keV, $P_{Ar^+}=2\times10^{-6}$ mbar) for 1 h to remove the contaminants. Then the surface was annealed at 900 °C for a few minutes to recover a crystalline surface. The Co was evaporated *in situ* with an electron bombardment deposition cell (EFM4 from Omicron) with a high purity rod of Co (99.99%). The Co flux, around 0.1 ML/h, was calibrated with a quartz microbalance and the pressure was kept below 10^{-9} mbar during deposition. To study the surface topography and the growth of Co at room temperature (RT), *in situ* GISAXS measurements were performed at the European Synchrotron Radiation Facility (ESRF, Grenoble, France) using the UHV surface diffraction setup of the BM32 bending magnet beamline.[15] The sample is mounted vertically on the head of a six-circle diffractometer ("z-axis type") which holds the UHV chamber (base pressure of 1×10^{-10} mbar). The x-ray beam was sagitally focused on the sample with horizontal $H=0.4$ mm and vertical $V=0.3$ mm sizes (full width at half maximum, FWHM), corresponding to divergences of $\delta_H=1$ mrad and $\delta_V=0.13$ mrad, respectively. The incident x-ray beam of 18 keV energy ($\lambda=0.06888$ nm) was used under grazing incidence, at the critical angle of Au ($\alpha_i=\alpha_c=0.25°$). The intensity scattered by the surface has been collected at wide angles (GIXD) with a standard NaI detector. The vertical acceptance was set to 0.2° for the in-plane scans. For GIXD measurements, the hexagonal surface unit cell of the terrace plane is used ($A=B=a/\sqrt{2}$). $\vec{C}$ is aligned along the [111] direction ($C=a\sqrt{3}$), where the indices refer to the fcc unit cell and a (0.4078 nm) is the lattice parameter of Au. The corresponding reciprocal coordinates (HKL) are defined in the $(\vec{A}^*,\vec{B}^*,\vec{C}^*)$ basis (see Fig. 1). GISAXS images have been collected on a high grade 16-bit charge coupled device camera (1152×1252 pixels, pixel size 56.25×56.25 μm^2) at a sample distance of 0.885 m. The out-of-plane exit angles and the in-plane exit angles were ranging, respectively, between 0 and 4.6° for α_f and between −2.1° and +2.1° for $2\theta_f$. They allow us to define the wave vector transfer coordinates (q_x,q_y,q_z) through[16,17]

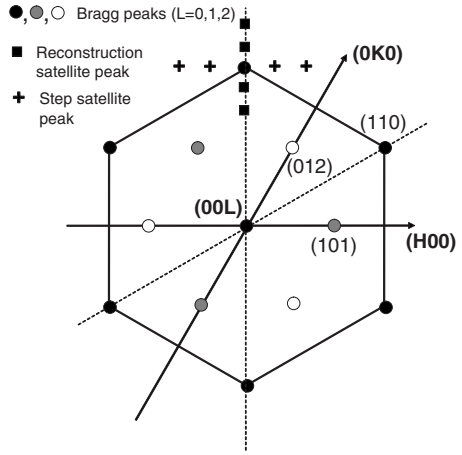

FIG. 1. Schematic representation of the reciprocal space of a vicinal surface of Au(111) tilted in the $[\bar{2}11]$ direction in the $L=0$ plane. ($H00$) and ($0K0$) are the axes of the reciprocal space in the surface plane of the hexagonal lattice of Au(111). The reciprocal space nodes of Au are represented with circles, and indexed with respect to the bulk Au fcc unit cell. The satellite nodes of the reconstruction and the step network are schematically shown as squares and crosses around the $(\bar{1}20)$ Bragg peak.

$$q_x = k_0[\cos(\alpha_f)\cos(2\theta_f) - \cos(\alpha_i)],$$

$$q_y = k_0[\cos(\alpha_f)\sin(2\theta_f)],$$

$$q_z = k_0[\sin(\alpha_f) + \sin(\alpha_i)],$$

$$k_0 = 2\pi/\lambda. \tag{2.1}$$

The transmitted and specularly reflected beams were hidden by beamstops and guard slits implemented inside the UHV chamber.[18] The recording time for GISAXS measurements was typically a few minutes. The STM images were obtained on the same substrate in the constant current mode with a tunneling current of 1 nA using a positive voltage of 1 V.

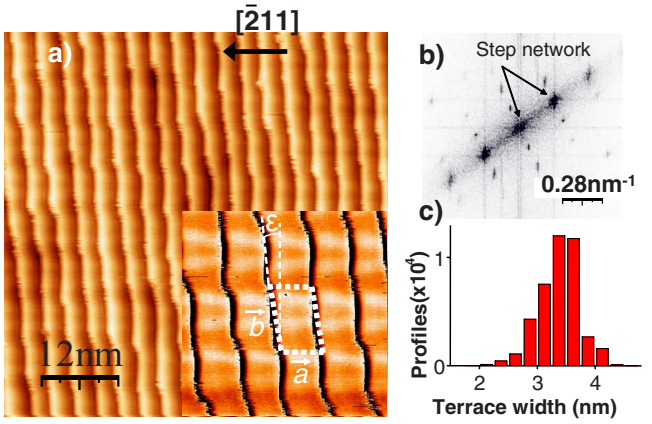

FIG. 2. (Color online) (a) STM image of the kinked Au(677) surface. Inset: Zoom on the surface, where the vicinal staircase has been subtracted numerically to highlight the double stacking fault lines of the reconstruction. $\vec{a}$ and $\vec{b}$ are the base vectors of the unit cell. The kinks are visible as diffuse and tilted area. The angular offset ε between the average step direction and the [0$\bar{1}$1] direction is $5 \pm 1°$. (b) Fourier transform of an image. Both period of the step network and the reconstruction and/or kinks are put in evidence. (c) Histogram of the terrace width performed over 20 000 profiles.

III. SCANNING TUNNELING MICROSCOPY AND GRAZING INCIDENCE SMALL-ANGLE X-RAY SCATTERING STUDY OF THE KINKED Au(677) SURFACE

A. Scanning tunneling microscopy measurements

The kinked Au(677) surface that we have studied (see Fig. 2) is very similar to the Au(788) surface, which has already been described in previous papers (see for instance, Ref. 8). The surface is nominally tilted with respect to the [111] crystallographic orientation by an angle of 4° in the [$\bar{2}$11] direction (the indices refer to the fcc unit cell of Au). It is made of a regular staircase of monatomic steps (0.235 nm in height) and 3.4 nm wide terraces. Similar to the Au(111) surface, the terraces are reconstructed.[19] However, only one variant of the reconstruction is observed, due to an energetic raised degeneracy thanks to the symmetry breaking induced by the steps. This reconstruction is visible in the STM images as double lines,[19] aligned perpendicularly to the step edges, in the [$\bar{2}$11] direction [see Fig. 2(a), inset]. They reveal the presence of stacking faults between domains of fcc and hcp crystallographic structures as already seen in the case of the Au(788) surface.[8,7]

The step edges are slightly disoriented with respect to the [0$\bar{1}$1] direction, which leads to the occurrence of kinks at the step edges as seen by STM [see Fig. 2(a)]. A close view reveals that they are not monatomic kinks, but they pack periodically and make tilted and diffuse areas. The STM images show that the kinks are trapped in between the stacking fault lines, inside the fcc stacking areas, and are, therefore, excluded from the hcp areas, which implies that the kinks are ordered and follow the terrace reconstruction periodicity. One can also notice the fuzzy aspect of kinks, which is an indication of the mobility at RT of Au atoms along the step edges.[20] A parallelogram unit cell at the nanometer scale can be drawn from the previous analysis [see Fig. 2(a), inset] with two nonorthogonal basis vectors $\vec{a}$ and $\vec{b}$. $\vec{a}$ is in the [$\bar{2}$11] crystallographic direction, and the length is equal to the terrace width. $\vec{b}$ is parallel to the mean step edge direction, i.e., slightly misoriented (angular offset ε) with respect to the [0$\bar{1}$1] crystallographic direction because of the kinks. The modulus of $\vec{b}$ is equal to the reconstruction period. The corresponding reciprocal space coordinate (hkl), for the GISAXS experiments, are defined in the ($\vec{a}^*$,$\vec{b}^*$,$\vec{c}^*$) basis where $\vec{c}^*$ is perpendicular to the mean surface plane ($|\vec{c}^*| = 1$ nm^{-1}).

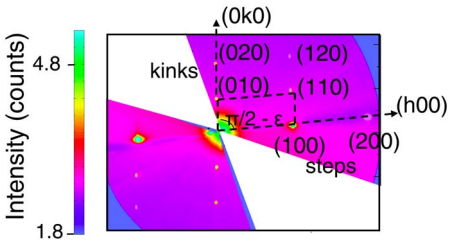

FIG. 3. (Color online) Experimental map of the reciprocal space in the surface plane of the kinked vicinal surface of Au(111). The angular offset ε deduced from this map is $\varepsilon = 4.95°$.

B. Grazing incidence small-angle x-ray scattering measurements

To get quantitative information on the long-range order and the morphology of the kinks, *in situ* GISAXS measurements have been performed and analyzed in the light of these STM images. The intensity scattered by the surface has been measured over a three-dimensional volume of the reciprocal space in the small-angle regime: GISAXS patterns have been recorded at different azimuths, rotating the sample by steps of 1° over a large angular range (140°). In Fig. 3 a projection of the GISAXS intensity in the surface plane ($l=0$) is shown. The (10l) and (20l) scattering rods from the step network are visible, as well as (01l) and (02l) rods which arise from the kink long-range order and are rotated by $\pi/2-\varepsilon$. The angular offset ε arises from the rotation of the mean step edge orientation due to the kinks [see Fig. 2(a)]. We have also measured the higher order scattering rods (11l) and (12l) coming from both periodicities. It is, thus, necessary to develop a realistic model of the surface topography for which the intensity scattered by the surface can be calculated in three dimensions.

Two contributions have to be considered to evaluate the GISAXS intensity: the surface topography (steps and kinks) and the surface reconstruction. As the calculation is rather complex, it is useful to estimate the different contributions. The most important point is to compare the kinks and the reconstruction contributions, which have the same periodicity. A first rough estimation consists in considering the electronic density contrast involved in the scattering power by the kinks and by the reconstruction. The kink's contribution

can be estimated by measuring the difference between a straight monatomic step edge and a kinked one. From the angular misorientation ($\varepsilon = 5 \pm 1°$ from the STM images), there are three atomic kinks per period of the reconstruction, i.e., a discrepancy of ± 1.5 atomic row as compared with a straight step edge. The corresponding difference in the electronic density of a terrace is $\pm 10\%$ (size 3.4 nm, 14 atomic rows). Concerning the reconstruction, the in-plane variations of the electronic density can be estimated from previous x-ray reflectivity measurements on the Au(111) surface.[21] It has been shown that the mean in-plane contraction of the top layer is 4%. Thus, the expected in-plane variations of the electronic density are confined in the top layer (equal to the step height) and are about $\pm 2\%$. Since the scattered intensity is proportional to the square of the contrast in electronic density, the scattering by the reconstruction is about 25 times weaker than that from the kinks, and can be neglected. This is in agreement with preliminary GISAXS measurements performed under the same conditions on the Au(111) surface:[22] no intensity from the reconstruction was measurable. Supposing that the Au(111) reconstruction is similar to the Au(677) one, we can conclude that the kinks are responsible for the diffuse scattering observed at the periodicity of the reconstruction. A similar comparison concerns the contribution of steps to the scattered intensity. Is it the topography of the steps or the elastic strain fields generated by these defects that prevails in the small-angle scattering? A straight step is a one-dimensional object, whereas the induced strain field is bidimensional and propagates at large distances. However, the very small compressibility of Au, thanks to a Poisson coefficient close to 0.5 [0.412 (Ref. 23)], reduces the amplitude of the dilatation field generated by steps and, thus, the scattering power. Therefore, the step topography is predominant in the scattered intensity.

In conclusion, to first order, the intensity scattered at small angles by the kinked Au(677) surface can be evaluated by a topographic model only.

IV. MODEL OF STEPPED AND KINKED SURFACES BASED ON THE PARACRYSTAL DESCRIPTION

A. Introduction

Diffraction by surfaces that are not perfectly periodic is a classical problem in surface science. Since the pioneer work of Lent and co-workers,[24,25] the calculation of the intensity scattered by different kinds of surface topographies has been solved assuming e.g., generic terrace width distributions. The two-level model, the vicinal surface, and the rough surface are typical 2D morphologies for which the reciprocal space is known. These calculations have mainly focused on the scattering by the last atomic layer (helium atom scattering, low energy electron diffraction[26,27]). A more general model should consider (i) a 3D description, for instance, in view of the calculation of the intensity scattered by a kinked vicinal surface and (ii) a sensitivity to deep layers for the calculation of the diffraction by x ray. A model is proposed below that extends previous results to x-ray scattering and provides a 3D description of surfaces in the case of a kinked vicinal surface. Details of this approach are first given in the simple cases of the vicinal surface and the two-level model. Then an extension for the kinked vicinal surface is given.

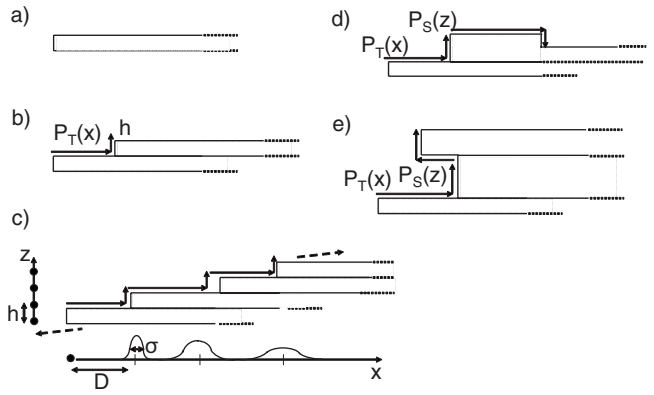

FIG. 4. Principle of the construction of a vicinal surface. (a) Elementary object: a semi-infinite rectangle of height h. (b) A second elementary object is shifted by a height h in the z direction and by a distance d (terrace width) in the x direction. d is given by a probability law $P_T(x)$ characterized by its mean value D and its standard deviation σ. (c) Step by step construction of the vicinal staircase. Below is shown a schematic representation of the probability density of the position of step edges with respect to the origin. (d) Vicinal surface assuming a positive step height distribution $P_S(z)$ for negative arguments (descending steps). (e) Vicinal surface assuming a positive terrace width distribution $P_T(x)$ for negative arguments (overhangs).

B. Vicinal surface

The analysis of a vicinal surface at the nanometer scale shows that despite disorder of the step positions, an elementary object without any size distribution[28] can be defined. It consists in a rectangle of monatomic height (h) starting at the step edge and semi-infinitely extended into the bulk (see Fig. 4). This object repeats according to a distribution law in order to describe a whole vicinal staircase. That way the role played by the step structure can be distinguished from that played by the terrace width distribution. The intensity scattered by the vicinal surface is the product of the modulus of the form factor of the elementary object $\tilde{F}_{vicinal}(q_x, q_z)$ times the interference function, which can be modeled by a one-dimensional (1D) model of disorder such as the paracrystal[14,29] model $S(q_x, q_z)$:

$$I(q_x, q_z) = |\tilde{F}_{vicinal}(q_x, q_z)|^2 \times S(q_x, q_z). \tag{4.1}$$

The shape factor of the elementary object is

$$\tilde{F}_{vicinal} = \int_{-h/2}^{h/2} e^{iq_z z} dz \int_{-\infty}^{0} e^{iq_x x + \mu x} dx = \frac{-2i}{q_x q_z} \sin\left(\frac{q_z h}{2}\right), \tag{4.2}$$

where μ is the lineic absorption coefficient projected along the x axis. It is neglected in the following because it is usually very small compared to the momentum transfer studied by x-ray scattering.[30]

The interference function $S(q_x,q_z)$ is the Fourier transform of the autocorrelation function of the step positions $g(x,z)$. Within the paracrystal model, the step positions can be seen as a Markov chain. Each step position is determined from the position of its previous step and a terrace width distribution law, $P_T(x)$. This model predicts no long-range ordering; this is a cumulative disorder model:

$$S(q_x,q_z) = TF\{g(x,z)\},$$

$$S(q_x,q_z) = 1 + \{\tilde{P}_T(q_x)e^{iq_zh} + [\tilde{P}_T(q_x)e^{iq_zh}]^2 \ldots + \text{c.c.}\}, \tag{4.3}$$

where $\tilde{P}_T(q_x)$ is the Fourier transform of the terrace width distribution, and c.c. is the complex conjugate part. The sum converges because $|\tilde{P}_T(q_x)| \leqslant 1$, and yields

$$S(q_x,q_z) = Re\left\{\frac{1+\tilde{P}_T(q_x)e^{iq_zh}}{1-\tilde{P}_T(q_x)e^{iq_zh}}\right\}. \tag{4.4}$$

Therefore, the intensity reads

$$I(q_x,q_z) = \left[\frac{2}{q_xq_z}\sin\left(\frac{q_zh}{2}\right)\right]^2 Re\left\{\frac{[1+e^{iq_zh}\tilde{P}_T(q_x)]}{1-e^{iq_zh}\tilde{P}_T(q_x)}\right\},$$

$$I(q_x,q_z) = \frac{1}{(q_xq_z)^2}Re\left\{2\frac{(1-e^{iq_zh})[1-\tilde{P}_T(q_x)]}{1-e^{iq_zh}\tilde{P}_T(q_x)}\right\}. \tag{4.5}$$

The main advantage of this last expression[31] is to put in evidence the symmetric roles played by the terrace width and the step height distributions as e^{iq_zh} is the characteristic function of the step height distribution $P_S(z)$. This result can be generalized[28] for any step height distribution and reads

$$I(q_x,q_z) = \frac{1}{(q_xq_z)^2}Re\left\{2\frac{[1-\tilde{P}_S(q_z)][1-\tilde{P}_T(q_x)]}{1-\tilde{P}_S(q_z)\tilde{P}_T(q_x)}\right\}. \tag{4.6}$$

The prefactor $\frac{1}{(q_xq_z)^2}$ arises from two contributions. The $\frac{1}{q_z^2}$ term can be assigned to the truncation of the nominal surface (i.e., without step), the so-called crystal truncation rod, in the small-angle regime and the $\frac{1}{q_x^2}$ can be assigned to the truncation of a semi-infinite terrace by a step. Following Robinson,[32] it can be called terrace truncation rod. This prefactor can be generalized to wide-angle diffraction replacing $\frac{1}{(q_xq_z)^2}$ by $\frac{1}{[2\sin(q_xa/2)2\sin(q_zc/2)]^2}$ in the cubic case,[28] and considering distribution of spacing with discrete values (to keep the crystallographic lattice periodicity). To make sure that the vicinal surface is single valued, it is necessary to add a constraint on the distributions of terrace width and step height: they cannot be both strictly positive for negative arguments. However, one of the distributions can have negative arguments, e.g., a negative step height [see Fig. 4(d)] is simply a descending step (see Ref. 28). In the case of negative terrace width, overhangs happen, which are nonphysical situations for vicinal surfaces [see Fig. 4(e)], but this may be useful to describe fracture profiles.[33]

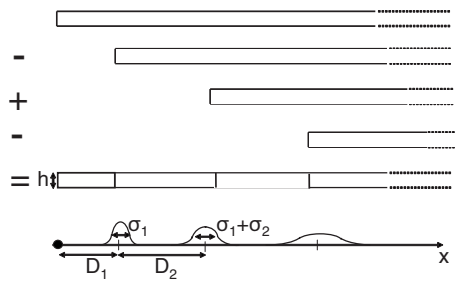

FIG. 5. Construction of the two-level model. The elementary object is identical to the one used for the vicinal surface, i.e., a semi-infinite rectangle of height h. The principle of the construction of the two-level model is to sum alternatively this object and its opposite shifted along the x direction. The probability law may depend on the nature of the object.

As an example, for a fixed step height and a Gaussian terrace width distribution:

$$P_T(x) = \frac{1}{\sqrt{2\pi\sigma}}e^{-(x-D)^2/2\sigma^2}, \quad P_S(z) = \delta(z-h),$$

where D and σ are, respectively, the mean terrace width and the standard deviation. $\tilde{P}_T(q_x)$ and $I(q_x,q_z)$ read explicitly

$$\tilde{P}_T(q_x) = \Phi e^{iq_xD} \quad \text{with } \Phi = e^{-(q_x\sigma)^2/2}$$

$$I(q_x,q_z) = \left[\frac{2}{q_xq_z}\sin\left(\frac{q_zh}{2}\right)\right]^2 \frac{1-\Phi^2}{1+\Phi^2-2\Phi\cos(q_zh+q_xD)}. \tag{4.7}$$

In the previous expression, the phase term $\cos(q_zh+q_xD)$ shows that the scattering rods are tilted with respect to the terrace plane and aligned perpendicular to the macroscopic surface plane. Before studying the kinked vicinal surface model, a second classical example, the two-level model, can be solved with the same approach.

C. Two-level model

The two-level model allows us to evaluate the intensity scattered by a smooth surface. The roughness is modeled by the alternation of upward and downward steps (see Fig. 5). Choosing as elementary object the same as for the vicinal surface $\tilde{F}_+(q_x,q_z)$, i.e., a semi-infinite rectangle starting at the step edge, the two-level model can be built, alternating on the surface this elementary object and its exact opposite, $\tilde{F}_-(q_x,q_z) = -\tilde{F}_+(q_x,q_z)$:

$$\tilde{F}_\pm(q_x,q_z) = \pm\frac{2i}{q_xq_z}\sin\left(\frac{q_zh}{2}\right). \tag{4.8}$$

To describe the spatial arrangement of upward and downward steps, we use the 1D-paracrystal model where the nodes are alternatively filled by the elementary object and its opposite. Writing down respectively $\tilde{P}_+(q_x)$ and $\tilde{P}_-(q_x)$ the characteristic functions of the up $z=+h/2$ and down $z=-h/2$ terrace width distributions, the intensity for off-specular scattering[28] ($q_x \neq 0$) reads

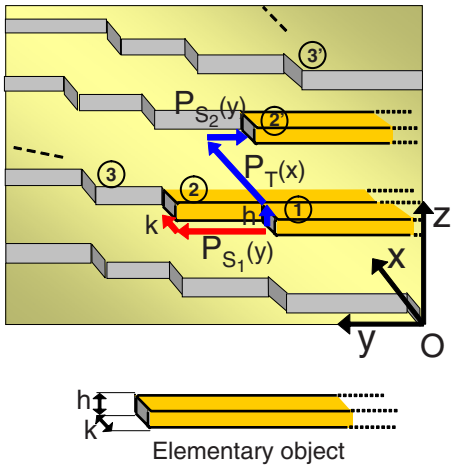

FIG. 6. (Color online) Scheme of the principle of the construction of a kinked vicinal surface (fixed kink and step dimensions). Elementary object: a parallelepiped of height h, width k, and semi-infinitely extended in the y direction. The surface is built similarly to the vicinal surface, adding step by step elementary objects along two directions: along the step edges (object 1, 2, 3,…) and perpendicular to the steps (object $1,2',3',\ldots$). A probability law $P_{S_1}(y)$ provides the distance distribution between the kinks at the step edges, and two probability laws give the terrace width $P_T(x)$ and the relative displacement in the y direction of two neighboring kinks at adjacent step edges, $P_{S_2}(y)$.

$$I(q_x,q_z)=\left[\frac{2}{q_xq_z}\sin\left(\frac{q_zh}{2}\right)\right]^2 Re\left\{\frac{[1-\tilde{P}_+(q_x)][1-\tilde{P}_-(q_x)]}{1-\tilde{P}_+(q_x)\tilde{P}_-(q_x)}\right\}. \tag{4.9}$$

This result is in agreement with previous results of Pukite *et al.* (see Ref. 25) and Croset and de Beauvais (see Ref. 27), except for the additional prefactor $\frac{1}{q_z^2}$ which corresponds to the contribution of deep layers. The $\frac{1}{q_z^2}$ is, in fact, the crystal truncation rod term[32] in the small-angle regime. It can be generalized to $\left[\frac{1}{2\sin(q_zh/2)}\right]^2$ assuming the discrete nature of the crystallographic lattice perpendicular to the surface. To make sure that the two-level model is single valued, it is necessary to choose $P_+(x)\geqslant 0$ and $P_-(x)\geqslant 0$.

D. Kinked vicinal surface

To simplify, we consider first a kinked vicinal surface with a fixed step height, h, and a fixed kink lateral size, k. As for the vicinal surface, one has to find an elementary object that repeats regularly on the surface. This object is a semi-infinite row parallel to a step edge, starting at a kink site and going into the bulk of the material along the y axis. It can be modeled as a semi-infinite parallelepiped of height h and lateral size k (see Fig. 6). Its form factor reads

$$\tilde{F}_{\text{kinked vicinal}}=\int_{-h/2}^{h/2}e^{iq_zz}dz\int_{-k/2}^{k/2}e^{iq_xx}dx\int_{-\infty}^{0}e^{iq_yy+\mu y}dy$$
$$=\frac{-4i}{q_xq_yq_z}\sin\left(\frac{q_zh}{2}\right)\sin\left(\frac{q_xk}{2}\right). \tag{4.10}$$

A more detailed atomic structure of the kinks can be considered. However, the GISAXS technique is not sensitive to it, contrary to grazing incidence x-ray diffraction for which a precise crystallographic description of the structure is necessary.

Then the kinked vicinal surface is built as an infinite assembly of these objects arranged along two main directions: along the step edge and perpendicular to the steps, to take into account the spatial correlations between kinks from step to step. Both directions are decoupled by hypothesis and the kink positions are obtained through the ideal 2D-paracrystal model[14] assuming distance distributions between nearest neighbor kinks. The kink positions are obtained step by step from the probability law of the distance between the first neighbor kinks in the two main directions. This hypothesis is questionable because kinks interact via long-range interactions (e.g., elastic interaction). This problem exists also for steps for which there are correlations with far steps arising from elastic interactions. However, this makes the analysis much more complex and our purpose is to give an analytical calculation of the intensity scattered by a kinked vicinal surface assuming generic distance distributions between first neighbors steps and kinks. An appropriate choice of the probability distributions may allow us to take partially into account the long-range interactions. This model also ensures that single valuedness of the surface is strictly preserved in the building process.[28] This is true whatever the choice of the probability distribution. Indeed, at each step of the building process of the surface morphology, the elementary building blocks are shifted either along z (step height) or along x (kink width). Concerning overhangs, they can be avoided if the terrace width distribution and kink-kink distance distribution are null for negative arguments.[28]

In summary, we are in the simple case of an elementary object ordered along two directions modeled in the framework of the ideal 2D-paracrystal model. In the direction parallel to the mean step edge:

$$S_{\parallel}(q_x,q_y)=Re\left\{\frac{1+e^{iq_xk}\tilde{P}_{S_1}(q_y)}{1-e^{iq_xk}\tilde{P}_{S_1}(q_y)}\right\}, \tag{4.11}$$

where $\tilde{P}_{S_1}(q_y)$ is the characteristic function of the distance separating two nearest neighbor kinks along the step edge. This calculation is exactly the same as for the vicinal surface.

For the direction perpendicular to the step edges:

$$S_{\perp}(q_x,q_y,q_z)=Re\left\{\frac{1+e^{iq_zh}\tilde{P}_T(q_x)\tilde{P}_{S_2}(q_y)}{1-e^{iq_zh}\tilde{P}_T(q_x)\tilde{P}_{S_2}(q_y)}\right\}, \tag{4.12}$$

where $\tilde{P}_T(q_x)$ and $\tilde{P}_{S_2}(q_y)$ are, respectively, the characteristic functions of the terrace width distribution and of the distance distribution along y of two kinks on two adjacent steps (see Fig. 6).

The kinked surface of Au(677) under study is slightly more complex. From the STM images (see Fig. 2), it was clearly observed that many kinks are packed together. These multikinks are modeled as a large kink and a size distribution $P_K(x)$ instead of e^{iq_xk}. The previous result can be generalized

for any kink size distribution (fixed step height, h):

$$I(q_x,q_y,q_z) = \left[\frac{1}{q_x q_y q_z}\right]^2 2\,Re\left\{\frac{(1-\tilde{P}_{S_1})[1-\tilde{P}_K(q_x)]}{1-\tilde{P}_{S_1}\tilde{P}_K(q_x)}\right\} \times 2\,Re\left\{\frac{(1-e^{iq_z h})[1-\tilde{P}_T(q_x)\tilde{P}_{S_2}(q_y)]}{1-e^{iq_z h}\tilde{P}_T(q_x)\tilde{P}_{S_2}(q_y)}\right\}. \quad (4.13)$$

In summary, the total number of size distributions is 4. To give explicit expressions, they are modeled by Gaussian laws characterized by their first two moments, i.e., mean size and standard deviation. Gaussian distributions are commonly used because their Fourier transform is easy to compute. However, these distributions are not strictly equal to zero for negative arguments which correspond to nonphysical situations. We expect, in our case, that only small changes could be obtained considering more appropriate distributions because the distributions are narrow enough, which makes negative arguments highly improbable. From this model, it is possible to extract the kink size distribution $P_K(x)$, the kink-kink distance along the step edges $P_{S_1}(y)$, the terrace width distribution $P_T(x)$, and the distribution of distances along (Oy) of two kinks located on two neighboring step edges, $P_{S_2}(y)$. One can also notice the prefactor $\left[\frac{1}{q_x q_y q_z}\right]^2$. It arises from the truncation of the semi-infinite flat crystal, $\frac{1}{q_z^2}$; the truncation of a semi-infinite terrace by a step, $\frac{1}{q_x^2}$; and the truncation of a semi-infinite step edge by a kink, $\frac{1}{q_y^2}$, which can be called step truncation rod.[28]

V. QUANTITATIVE ANALYSIS OF GRAZING INCIDENCE SMALL-ANGLE X-RAY SCATTERING FROM A STEPPED AND KINKED SURFACE

The principle of the analysis is to fit the GISAXS intensity of a kinked Au(677) surface thanks to the previous model. In comparison with Eq. (4.13), a rotation of the coordinates of reciprocal space is necessary since GISAXS experiments are performed at constant incident angle with respect to the average surface plane, which is tilted compared to the terrace plane. The azimuth angle is ω (ω=0 corresponds to an incident beam aligned along the mean step edge orientation, see Fig. 7). Then the morphological parameters are obtained by fitting the experimental data. The fit procedure uses the ISGISAXS software[17] using a χ^2 criterion, with error bars proportional to the square root of the intensity. As the experiment has been performed under grazing incidence, i.e., at the critical angle of Au, the simulations must be performed in the framework of the distorted-wave Born approximation[13,34] (DWBA), considering the kinked vicinal surface morphology as roughness. The reference plane is a planar Au surface. In the framework of this model, the intensity is proportional to the square moduli of the Fresnel transmission coefficients of Au at the angles of incidence and emergence multiplied by the square modulus of the form factor of the kinked vicinal surface [Eq. (4.13)], but changing the vertical component of the momentum transfer due to the refraction at the vacuum/Au interface. The model is able to reproduce all the features of the reciprocal space, i.e., the scattering rods from the steps, the kinks, and higher order terms. Thus, all the parameters have been fitted simultaneously using all the data set. GISAXS patterns have been collected at many azimuths, providing a 3D measurement close to the origin of the reciprocal space. Only a fraction of this huge data set could be used for the fit. For that sake, cross sections of intensity have been extracted from different GISAXS images (see Fig. 7): 15 cross sections have been used corresponding to the (10l) scattering rods (from the steps), 13 arise from the (01l) scattering rods of the kink network, and 11 from a higher order scattering rod, i.e., the (11l). Such a large amount of data constrains the parameters of the model. Although, in principle, the results cannot be dissociated, fits of the different rods are represented separately. Note that the relative amplitude of the scattering rods is well reproduced by the model, more particularly, the 2 orders of magnitude between the intensity of the scattering rods.

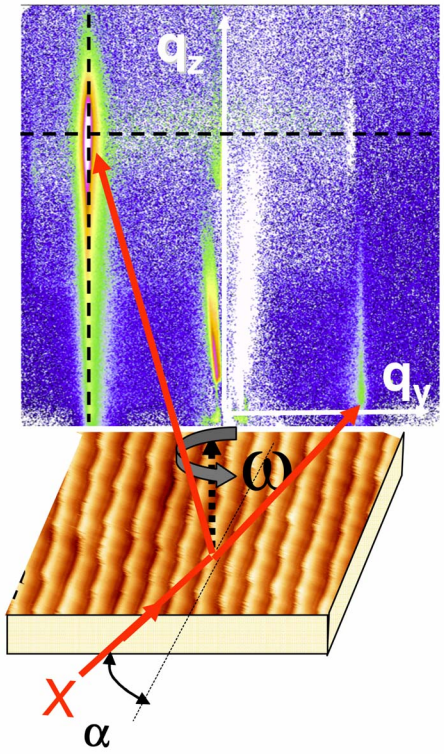

FIG. 7. (Color online) Example of a GISAXS pattern. α is the incident angle perpendicular to the surface; ω is the in-plane orientation (azimuth angle) of the incident x-ray beam with respect to the average step direction. Here, the x-ray beam is offset by ω=6° with respect to the mean step edge direction. The scattering rod arising from the step network crosses the Ewald sphere at large out-of-plane angle. Two cross sections (dotted lines) of intensity are extracted from this 2D map to fit the parameters of the model.

A. Scattering rods from periodic steps

The main characteristic feature of the intensity scattered by the steps is the asymmetry between the (10l) and ($\bar{1}$0l)

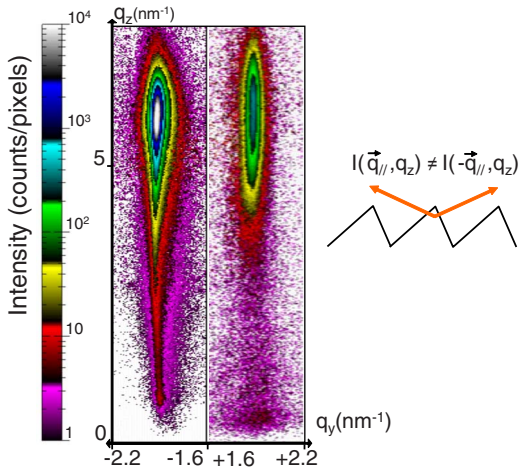

FIG. 8. (Color online) Portion of two GISAXS images measured for two symmetric azimuth angles ($\omega = \pm 6°$) with respect to the mean step edge orientation. The asymmetry of the scattering rods is clearly put in evidence.

scattering rods (see Fig. 8). It arises from the lack of mirror symmetry of the surface topography and the effect is all the more pronounced as l is large, i.e., far from the condition of application of Friedel's law.[35]

The experimental data and the simulated ones after fitting the parameters are shown in Fig. 9. The agreement is good except at large out-of-plane exit angle (α_f), where the model predicts a too large intensity. This can be explained by the roughness at the step edges (the terraces are smooth), which is not included in the model. Such roughness would induce a

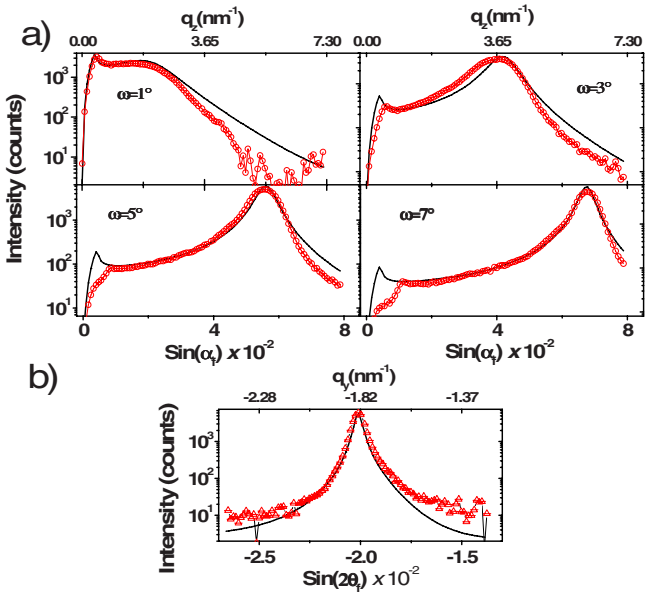

FIG. 9. (Color online) Fitted and experimental cross sections of the scattering rods by the step network. (a) Experimental (○) and fitted (solid line) cross sections integrated parallel to the surface plane for azimuth close to the mean step edge orientation. (b) GISAXS cross section parallel to the surface plane (△) and fit (solid line) for $\omega = 5°$.

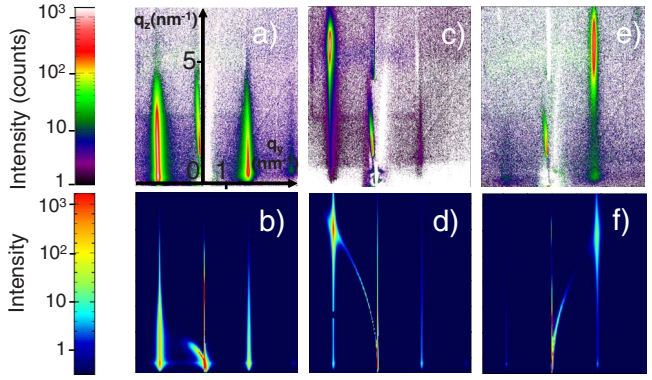

FIG. 10. (Color online) [(a), (c), and (e)] Experimental GISAXS patterns and [(b), (d), and (f)] simulated ones for different azimuthal orientations of the incident beam. In (a) and (b), the beam is aligned along the mean step edge orientation, $\omega = 0°$. In (c) and (d), the misorientation angle is $\omega = +5°$. In (e) and (f), $\omega = -5°$.

damping of the intensity for increasing q_z and, therefore, improve the fit at large l. The second discrepancy with the experimental data comes from the position and the intensity of the so-called Yoneda peak.[36] From the DWBA theory, an increase of the intensity should occur when the emergence angle is equal to the critical angle of Au (0.25°). An increase of the intensity followed by a maximum is, indeed, observed at small exit angles, but not at the expected position, and moves as a function of the azimuth angle. This discrepancy is all the more pronounced as the incident beam is rotated from the mean step edge orientation. This shows that a more rigorous DWBA theory is probably needed to precisely describe the intensity scattered by well-ordered surfaces at very small exit angles. Note, however, that, except at these locations where multiple scattering is predominant, the fit is correct. From the fitted parameters, complete 2D GISAXS patterns have been simulated for different azimuths (see Fig. 10) to check the validity of the model. Most of the scattered intensity is very well reproduced except for a curved scattering rod, which is simulated but does not appear in the data. It can be attributed to the terrace truncation rod term in the model. This discrepancy comes from the step edge roughness which is not properly taken into account, and which should attenuate the intensity very quickly. From the fit, the main extracted parameters are the mean terrace width and the standard deviation.

B. Scattering rods from periodic kinks

The FWHM of the (01l) scattering rods arising from the kink network is extremely small. This indicates a long-range ordering of the kinks (200 nm), which confirms the essential role played by the surface reconstruction that traps the kinks (see Fig. 11). For the same reason as for the steps, i.e., the lack of mirror symmetry of the surface, the scattering rods from the kink network are also asymmetric. The intensity is about 1 order of magnitude smaller than for the step network.

After the fit procedure, the scattering rods are well reproduced by the simulations (see Figs. 11 and 12). The most

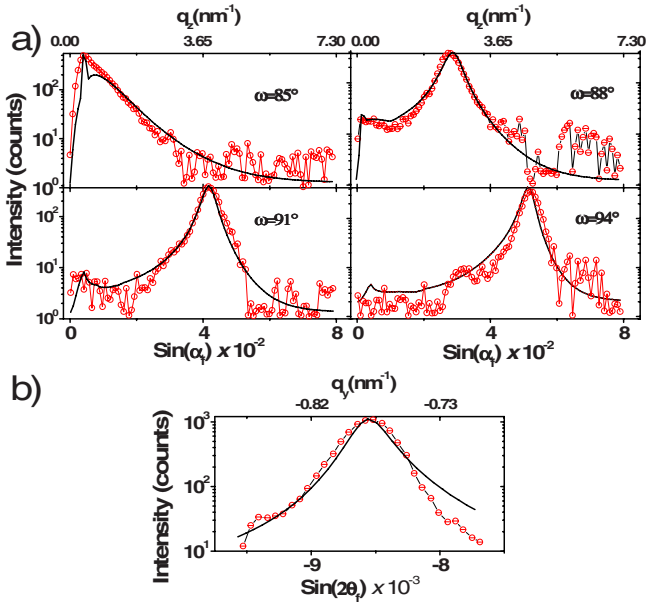

FIG. 11. (Color online) Fit and experimental cross sections of the scattering rods arising from the kink network. (a) Experimental (○) and fitted (solid line) cross sections integrated parallel to the surface plane for azimuth close to the $[\bar{2}11]$ direction (ω=85°). (b) Cross section parallel to the surface plane (⊖) and fit (solid line). The azimuth angle is ω=94°.

sensitive parameters of the fit for these scattering rods are the mean kink-kink distance along the step edges as well as the standard deviation of the distribution.

C. Higher order term: The (11*l*) crossed scattering rod

The intensity of the (11*l*) scattering rod has not been used to fit the parameters because the model was already constrained enough, and all information were obtained on other rods. Despite that, a very good agreement between the simulations and the experimental (11*l*) is found (see Figs. 13 and 14). The quality of the fit is highlighted by the fact that 2 orders of magnitude separate the intensity of the (10*l*) scattering rods of the step network and the intensity of the (11*l*) scattering rod.

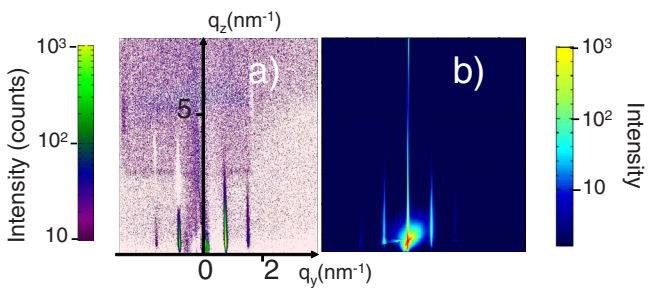

FIG. 12. (Color online) (a) Experimental GISAXS pattern and (b) simulation for the scattering rods arising from the kink network (ω=85°).

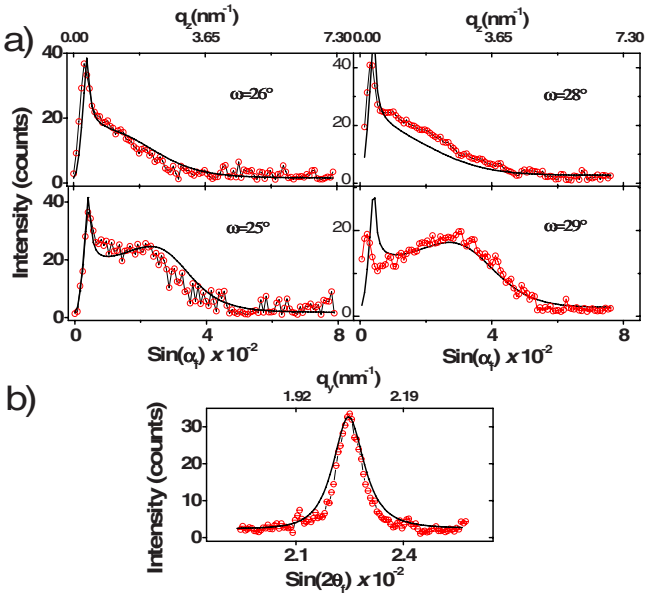

FIG. 13. (Color online) (a) Fit (solid line) and experimental (○) cross sections of the (11*l*) and $(\bar{1}1l)$ scattering rods (respectively, ω=28°,29° and ω=25°,26°). The cross sections are integrated parallel to the surface plane. (b) Cross section parallel to the surface plane (⊖) and fit (solid line). The azimuth angle is ω=29°.

D. Comparison of scanning tunneling microscopy and grazing incidence small-angle x-ray scattering results

The results deduced from the fit procedure are synthesized in Table I. The angular misorientation of the mean step edge with the $[\bar{1}10]$ direction determined by GISAXS is 4.95°. It is smaller than the one deduced from the STM images ($\sim 5 \pm 1$°) because the misorientation angle is precisely defined on a macroscopic scale and not on a local scale, and the determination of the crystallographic $[\bar{1}10]$ direction is difficult. The mean terrace size is 3.42 nm, in good agreement with the one obtained by STM. The standard deviation of the terrace width distribution (0.23 nm) is about twice smaller than the one deduced from the STM data (0.5 nm). This difference arises mainly from the different definitions of the terrace width distributions. For the STM analysis, the terrace width distribution includes the fluctuations of the step-step distance (assuming straight lines), the fluctuations of the kink positions, and the fluctuations of their size. The quantitative

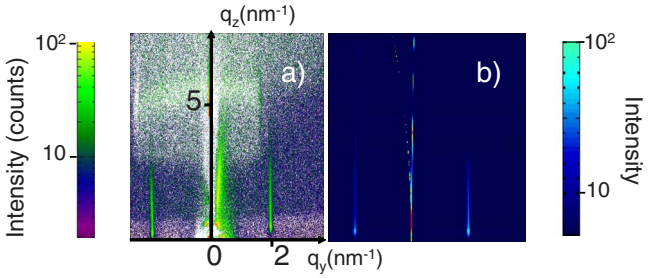

FIG. 14. (Color online) (a) Experimental GISAXS pattern and (b) simulation for the (11*l*) and $(\bar{1}1l)$ scattering rods (ω=27°).

TABLE I. Topographic parameters of the kinked Au(677) surface deduced from the quantitative analysis of GISAXS data. The step height is fixed at 0.235 nm. The values deduced from STM images are in brackets.

Kink size			Kink-kink distances					
			Step P_{S_1}		Terrace P_T		Kink P_{S_2}	
Width (nm)	Distribution (nm)	Height (nm)	S_1 (nm)	σ_{S_1} (nm)	T (nm)	σ_T (nm)	S_2 (nm)	σ_{S_2} (nm)
0.7	0.35	0.235	8.04 (8.0)	0.62	3.42 (3.4)	0.23 (0.5)	0	0.3

analysis of the GISAXS data makes the distinction between these three contributions. By combining these three broadening effects, the STM value is recovered.

The specific parameters that can be deduced from the GISAXS analysis are the following: the kink size is 3 ± 1.5 monatomic kinks that are packed together. They are well ordered along two directions: (i) From step to step, the kink distance is $T=3.42$ nm (mean terrace size), with a standard deviation $\sigma_T=0.23$ nm. The relative position of two neighbor kinks along two adjacent step edges is centered around zero ($S_2=0$ nm) with a very narrow distribution ($\sigma_{S_2}=0.3$ nm). Thus, the kinks are aligned perpendicular to the steps. This result illustrates the crucial role of the reconstruction, which induces the ordering of the kinks from step to step [see Fig. 2(a), inset]. (ii) In the direction parallel to the step edges, the kinks are ordered according to the period of the reconstruction, $S_1=8.04$ nm, with a standard deviation σ_{S_1} of 0.62 nm. The period of the kink's position (i.e., the period of the reconstruction) is larger than the one observed on Au(111) vicinal surfaces with smaller miscut angles:[7] 6.3, 7, 7.2, and 8.0 nm, respectively, for the Au(111), (11 12 12), (788), and (677) surfaces. This reveals that steps, and at some points, kinks, give additional possibilities to the surface to relieve the surface stress[9,37] and, therefore, the periodicity increases.

VI. GROWTH OF Co CLUSTERS STUDIED BY GRAZING INCIDENCE SMALL-ANGLE X-RAY SCATTERING

The GISAXS study of the Co growth has been performed in real time, without interruption of the deposit. A qualitative understanding of the evolution of the intensity as a function of deposition time gives an insight on the growth process. Initially, the intensity decreases on the $(10l)$ scattering rod (step array) and increases on the $(01l)$ scattering rod (kink array). Only interference effects between the waves scattered by the surface and the Co clusters can explain these effects: the waves scattered by the Co clusters interfere destructively with those scattered by the steps, and constructively with those scattered by the kinks. Therefore, the Co clusters grow at the step edges and in between two kinks, which is in agreement with STM images of the growth of Co on Au(788).[7] To extract more information on the Co growth, the interference effects have to be interpreted more precisely. A statistical model of the surface topography and the Co clusters has to be developed to simulate the GISAXS patterns. However, the previous model, developed for the bare surface, cannot be applied for supported Co clusters in a straightforward way. The basic idea is to use another elementary object. A semi-infinite parallelepiped such as that used for the bare surface can be used with an additional Co cluster on top at a given position (see Fig. 15). No size distribution is included in the model (fixed kink size, fixed step height, and fixed Co cluster shape and size). That way the surface is entirely built considering this elementary object and two main directions for the periodicity. The intensity reads

$$I(q_x,q_z) = \left| \frac{-4i}{q_x q_y q_z} \sin\left(\frac{q_z h}{2}\right)\sin\left(\frac{q_x k}{2}\right) + \tilde{F}_{\mathrm{Co}} e^{i(q_x V - q_y U)} \right|^2 Re\left\{ \frac{[1+e^{iq_x k}\tilde{P}_{S_1}(q_y)]}{[1-e^{iq_x k}\tilde{P}_{S_1}(q_y)]} \right\} \times Re\left\{ \frac{[1+e^{iq_z h}\tilde{P}_T(q_x)\tilde{P}_{S_2}(q_y)]}{[1-e^{iq_z h}\tilde{P}_T(q_x)\tilde{P}_{S_2}(q_y)]} \right\}, \tag{6.1}$$

where $\tilde{F}_{\mathrm{Co}}$ is the form factor of the Co clusters, and U and V are their relative positions from the kink site, respectively, along the directions (Oy) and (Ox) (see Fig. 15). The Co cluster model is based on the analysis of the growth of Co on Au(788) at RT.[38,39] It has been shown that the clusters have approximately a cylindrical shape with an elliptic base and a fixed height (2 ML) (see Fig. 15). The form factor of the Co clusters is

$$\tilde{F}_{\mathrm{Co}}(q_x,q_y,q_z) = 2\pi DLH \frac{J_1[\sqrt{(q_x D/2)^2+(q_y L/2)^2}]}{\sqrt{(q_x D/2)^2+(q_y L/2)^2}} \frac{\sin(q_z H/2)}{q_z H/2}, \tag{6.2}$$

where J_1 is the Bessel function of the first kind (first order).

The results of the fits show good agreement between the simulated GISAXS patterns and the experimental ones (see Fig. 16). The morphological parameters of the Co clusters can be estimated as well as their position relative to the kink sites (Table II).

The results are also in good agreement with the STM experiments performed on the Au(788) surface. Note that although the position V of the cluster center with respect to the step edge varies, we find that the cluster edge always touches the step edge, as shown in Fig. 15(c). This result is in agreement with previous STM experiments on Au(788)

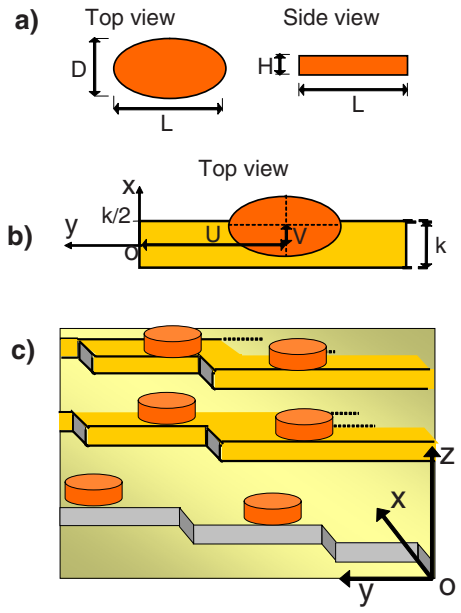

FIG. 15. (Color online) (a) Co clusters are modeled by cylinders with an elliptic base to take into account their shape anisotropy. Their height is fixed at 2 ML. (b) The elementary object is built as the superposition of a semi-infinite parallelepiped and a Co cluster on top, the position of which can be adjusted. (c) The order is modeled by an ideal 2D paracrystal. The main directions are the step edge and perpendicular to the steps.

that have shown that the clusters nucleate at the upper step edge and grow toward the center of the terrace. The clusters are anisotropic and are elongated along the step edges, which is typical of the growth at room temperature.[39]

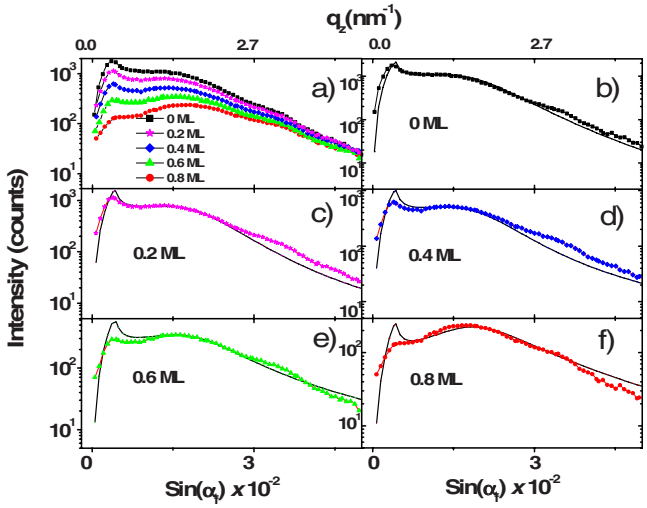

FIG. 16. (Color online) Experimental data and fit of the (10l) scattering rods from the step array during the growth of Co ($\omega = 0°$). The incident beam is aligned parallel to the mean step edge direction. (a) Time evolution of the scattering rod intensity integrated parallel to the surface plane. (b)–(f) Experimental data (○) and fit (solid line) at different amounts of Co on the surface.

TABLE II. Morphological parameters of the Co clusters deduced from the fit. H has been fixed at 0.4 nm (2 ML height) and U at 4.02 nm (i.e., the Co clusters are in between the kinks).

Deposit (ML)	D (nm)	L (nm)	H (nm)	U (nm)	V (nm)
0.2	1.2	1.2	0.4	4.02	0.25
0.4	1.4	2	0.4	4.02	0.35
0.6	1.6	2.7	0.4	4.02	0.4
0.8	1.7	3.3	0.4	4.02	0.45

VII. GROWTH OF Co CLUSTERS STUDIED BY GRAZING INCIDENCE X-RAY DIFFRACTION

GIXD measurements have been performed at RT for different stages of the Co growth, i.e., from the bare surface to a 15 ML thick film of Co. At the very beginning of growth, scans around the $(\bar{1}\ 2\ 0)$ and $(\bar{2}\ 0\ 5/2)$ coordinates of the hexagonal basis $(\vec{A}^*, \vec{B}^*, \vec{C}^*)$ reveal the period of the reconstruction [see Figs. 17(a) and 17(b)]. The period is in perfect agreement with GISAXS results. As the amount of Co increases, the characteristic satellite peaks arising from the reconstruction period disappear progressively. However, more than 3 ML of Co are necessary to suppress the reconstruction. It shows that the reconstruction on the kinked Au(677) is more robust than on the Au(111) surface, which disappears after only 1 ML of Co.[40] Concerning the step period, scans in the (H 1 1/2) direction cross the scattering rods of the step network in anti-Bragg conditions [see Fig. 17(c)]. The period deduced from the peak spacing is compatible with the value

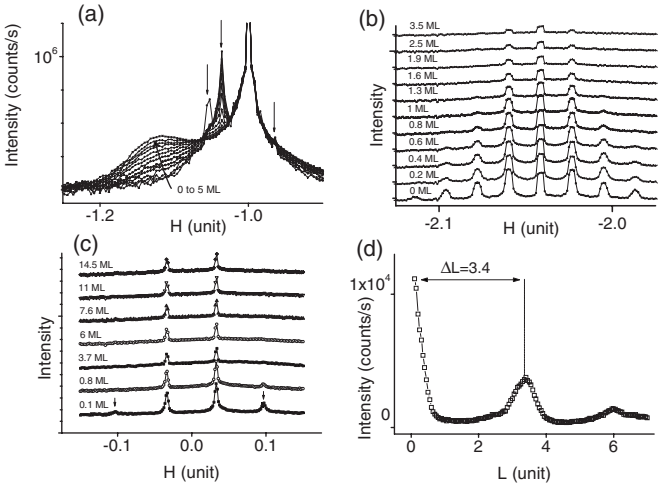

FIG. 17. (a) GIXD scans measured along the ($\bar{H}$ 2H 0.1) direction for increasing coverage of Co. The satellite peaks of the reconstruction decrease continuously with coverage (see arrows) and a broad Bragg peak of Co increases. (b) Same as before for scans measured along the ($\bar{2}$+H $\overline{2H}$ 5/2) direction. (c) GIXD scans along the (H 1 1/2) direction, i.e., in anti-Bragg condition of the step network. (d) L scan at (1.128 2.256 L) for 5 ML of Co. The spacing between the first two peaks is about $\Delta L = 3.4$ indicating that Co is mainly fcc.

deduced from GISAXS measurements. As the amount of Co increases on the surface, the high order scattering rods are damped, showing that the Co clusters roughen/strain the step edges. However, at 3 ML of Co, the two main peaks of the step array do not decrease anymore, revealing that the stepped structure of the underlying Au surface is kept even at large coverage.

Concerning the Co crystallographic structure, a broad peak at $(1.13\ 2.26\ 0)$ is visible for a coverage of 1 ML [see Fig. 17(a)]. This suggests that the Co clusters are already partially relaxed at the beginning of growth. The peak position only slightly shifts as a function of deposit due to the relaxation of the lattice parameter toward the bulk value [peak position at $(1.15\ 2.3\ 0)$]. To extract information on the crystallographic stacking of Co, an L scan at the Co lattice parameter [see Fig. 17(d)] has been performed for 5 ML of Co. It shows a distinct peak at $L=3.4$, indicating that the Co film is mainly fcc as observed by Girard *et al.* on vicinal surfaces of Au(111).[41] Concerning the periodicity of the Co clusters on the surface, it is instructive to note that no characteristic feature, such as a Dirac comb, is visible on the Co diffraction peaks as expected from the long-range order measured by GISAXS. This result can be assigned to the incommensurability of Co and Au crystallographic structures and to the inhomogeneous strain field inside the Co clusters induced by the substrate. Therefore, the Co clusters look completely disordered from the GIXD data. Contrary to GISAXS, GIXD is sensitive to displacements at the atomic scale. This makes GISAXS and GIXD complementary tools for the study of self-organized systems since GISAXS provides information on the long-range order, and GIXD on the crystallographic structure.

VIII. CONCLUSION

The kink ordering on a stepped surface of Au(111) slightly disoriented azimuthally has been characterized *in situ* by STM and GISAXS. A volumetric measurement of the reciprocal space has been performed at small angles and analyzed in the framework of a dedicated model based on the 2D ideal paracrystal.[14] From the fit, a description of the bare surface has been deduced including the step network and the kinks at the step edges. The long-range order of the kinks is clearly put in evidence and assigned to their interaction with the surface reconstruction. They are trapped inside the fcc stacking areas of the surface, i.e., in between the stacking fault lines as shown by STM.

Concerning the growth of Co, the interference between the waves scattered by the surface and by the clusters allows us to localize the Co clusters at the step edges and between the kinks. Their size and shape could also be estimated as a function of coverage. Finally, *in situ* GIXD measurements have yielded complementary information on the crystallographic structure of the Au substrate and the Co clusters.

ACKNOWLEDGMENTS

We acknowledge the invaluable help of Marion Ducruet for sample preparations, Tobias Schülli during some measurements, Rémi Lazzari for discussions, as well as the ESRF and BM32 staff for beam availability.

*leroy@crmcn.univ-mrs.fr

[1] H. Brune, M. Giovanni, K. Bromann, and K. Kern, Nature (London) **394**, 451 (1998).
[2] P. Gambardella, A. Dallmeyer, K. Maiti, M. C. Malagoli, W. Eberhardt, K. Kern, and C. Carbone, Nature (London) **416**, 301 (2001).
[3] F. Leroy, G. Renaud, A. Letoublon, R. Lazzari, C. Mottet, and J. Goniakowski, Phys. Rev. Lett. **95**, 185501 (2005).
[4] H. Brune, Surf. Sci. Rep. **31**, 121 (1998).
[5] N. Weiss *et al.*, Phys. Rev. Lett. **95**, 157204 (2005).
[6] B. Voigtländer, G. Meyer, and N. M. Amer, Phys. Rev. B **44**, 10354 (1991).
[7] S. Rousset, V. Repain, G. Baudot, Y. Garreau, and J. Lecoeur, J. Phys.: Condens. Matter **15**, S3363 (2003).
[8] V. Repain, G. Baudot, H. Ellmer, and S. Rousset, Mater. Sci. Eng., B **96**, 178 (2002).
[9] P. Müller and A. Saùl, Surf. Sci. Rep. **54**, 157 (2004).
[10] V. Repain, J. M. Berroir, B. Croset, S. Rousset, Y. Garreau, V. H. Etgens, and J. Lecoeur, Phys. Rev. Lett. **84**, 5367 (2000).
[11] V. Repain, J. M. Berroir, S. Rousset, and J. Lecoeur, Europhys. Lett. **47**, 435 (1999).
[12] G. Renaud *et al.*, Science **300**, 1416 (2003).
[13] S. K. Sinha, E. B. Sirota, S. Garoff, and H. B. Stanley, Phys. Rev. B **38**, 2297 (1988).
[14] R. Hosemann and S. N. Bagchi, *Direct Analysis of Diffraction by Matter* (North-Holland, Amsterdam, 1962).
[15] R. Baudoing-Savois, M. De Santis, M. C. Saint-Lager, P. Dolle, O. Geaymond, P. Taunier, P. Jeantet, J. P. Roux, G. Renaud, and A. Barbier, Nucl. Instrum. Methods Phys. Res. B **149**, 213 (1999).
[16] C. Revenant, F. Leroy, R. Lazzari, G. Renaud, and C. R. Henry, Phys. Rev. B **69**, 035411 (2004).
[17] R. Lazzari, J. Appl. Crystallogr. **35**, 406 (2002).
[18] G. Renaud, M. Ducruet, O. Ulrich, and R. Lazzari, Nucl. Instrum. Methods Phys. Res. B **222**, 667 (2004).
[19] J. V. Barth, H. Brune, G. Ertl, and R. J. Behm, Phys. Rev. B **42**, 9307 (1990).
[20] S. Rousset, S. Gauthier, O. Siboulet, J. C. Girard, S. de Cheveigne, M. Huerta-Garnica, W. Sacks, M. Belin, and J. Klein, Ultramicroscopy **42**, 515 (1992).
[21] A. R. Sandy, S. G. J. Mochrie, D. M. Zehner, K. G. Huang, and D. Gibbs, Phys. Rev. B **43**, 4667 (1991).
[22] O. Fruchart *et al.*, Europhys. Lett. **63**, 275 (2003).
[23] J. Hirth and J. Lothe, *Theory of Dislocations* (Wiley, New York, 1982).
[24] C. S. Lent and P. I. Cohen, Surf. Sci. **139**, 121 (1984).
[25] P. R. Pukite, C. S. Lent, and P. I. Cohen, Surf. Sci. **161**, 39 (1985).
[26] M. Henzler, *The Study of Epitaxy with Spot Profile Analysis of LEED (SPA-LEED)*, Springer Series in Surface Science Vol. 11

(Springer, New York, 1988).
[27] B. Croset and C. de Beauvais, Surf. Sci. **384**, 15 (1997).
[28] F. Leroy, R. Lazzari, and G. Renaud, Surf. Sci. **601**, 1915 (2007).
[29] A. Guinier, *X-ray Diffraction in Crystals, Imperfect Crystals and Amorphous Bodies* (Dover, New York, 1963).
[30] I. K. Robinson and D. J. Tweet, Rep. Prog. Phys. **55**, 599 (1992).
[31] B. Croset and C. de Beauvais, Surf. Sci. **409**, 403 (1998).
[32] I. K. Robinson, Phys. Rev. B **33**, 3830 (1986).
[33] Jan Oystein Haavig Bakke, T. Ramstad, and A. Hansen, Phys. Rev. B **76**, 054110 (2007).
[34] M. Rauscher, T. Salditt, and H. Spohn, Phys. Rev. B **52**, 16855 (1995).
[35] M. Rauscher, R. Paniago, H. Metzger, Z. Kovats, H. D. Domke, J. Pfannes, J. Schulze, and I. Eisele, J. Appl. Phys. **86**, 6763 (1999).
[36] Y. Yoneda, Phys. Rev. **131**, 2010 (1963).
[37] B. Salanon and P. Hecquet, Surf. Sci. **412-413**, 639 (1998).
[38] V. Repain, G. Baudot, H. Ellmer, and S. Rousset, Europhys. Lett. **58**, 730 (2002).
[39] N. Witkowski, Y. Borensztein, G. Baudot, V. Repain, Y. Girard, and S. Rousset, Phys. Rev. B **70**, 085408 (2004).
[40] On the nominal Au(111) surface, preliminary GIXD measurements have shown that the satellite peaks of the reconstruction disappear after 1 ML of Co.
[41] Y. Girard, G. Baudot, V. Repain, S. Rohart, S. Rousset, A. Coati, and Y. Garreau, Phys. Rev. B **72**, 155434 (2005).